

Study of Failed CME Core Associated with Asymmetric Filament Eruption

Navin Chandra Joshi¹, Abhishek K. Srivastava¹

Aryabhata Research Institute of Observational Sciences (ARIES), Manora Peak
Nainital-263 002, India; navin@aries.res.in, njoshi98@gmail.com, aks@aries.res.in

Boris Filippov²

Pushkov Institute of Terrestrial Magnetism, Ionosphere and Radio Wave Propagation,
Russian Academy of Sciences, Troitsk, Moscow, Russia

Wahab Uddin¹

Aryabhata Research Institute of Observational Sciences (ARIES), Manora Peak
Nainital-263 002, India

Pradeep Kayshap¹

Aryabhata Research Institute of Observational Sciences (ARIES), Manora Peak
Nainital-263 002, India

Ramesh Chandra³

Department of Physics, D.S.B. Campus, Kumaun University, Nainital-263 002,
Uttarakhand, India

Received _____; accepted _____

¹Aryabhata Research Institute of Observational Sciences (ARIES), Manora Peak
Nainital-263 002, India; navin@aries.res.in, njoshi98@gmail.com, aks@aries.res.in

²Pushkov Institute of Terrestrial Magnetism, Ionosphere and Radio Wave Propagation,
Russian Academy of Sciences, Troitsk, Moscow, Russia

³Department of Physics, D.S.B. Campus, Kumaun University, Nainital-263 002, Uttarakhand, India

ABSTRACT

We present the multi-wavelength observations of asymmetric filament eruption, associated CME and coronal downflows on 2012 June 17-18 during 20:00-05:00 UT. We use SDO/AIA, STEREO-B/SECCHI observations to understand the filament eruption scenario and its kinematics. While LASCO C2 observations have been analyzed to study the kinematics of the CME and associated downflows. SDO/AIA limb observations show that the filament exhibits whipping like asymmetric eruption. STEREO/EUVI disk observations reveal a two ribbon flare underneath the south-eastern part of the filament that is most probably occurred due to reconnection process in the coronal magnetic field in the wake of the filament eruption. The whipping like filament eruption later gives a slow CME in which the leading edge and the core propagate respectively with the average speed of $\approx 540 \text{ km s}^{-1}$ and $\approx 126 \text{ km s}^{-1}$ as observed in the LASCO C2 coronagraph. The CME core formed by the eruptive flux-rope shows the outer coronal downflows with the average speed of $\approx 56 \text{ km s}^{-1}$ after reaching up to $\approx 4.33 R_{\odot}$. Initially, the core decelerates with $\approx 48 \text{ m s}^{-2}$. The plasma first decelerates gradually up to the height of $\approx 4.33 R_{\odot}$ and then starts accelerating downward. We suggest a self-consistent model of a magnetic flux rope representing the magnetic structure of the CME core formed by eruptive filament that lost its previous stable equilibrium when reach at a critical height. With some reasonable parameters, and inherent physical conditions the model describes the non-radial ascending motion of the flux rope in the corona, its stopping at some height, and thereafter the downward motion, which are in good agreement with the observations.

Subject headings: Sun: Corona - Sun: Filament - Sun: Magnetic field - Sun: Coronal

Mass Ejection

1. Introduction

Filaments/Prominences are the cool (10^4 K) and denser ($10^{10} - 10^{11} \text{cm}^{-3}$) plasma material embedded in the magnetic field of the ambient solar atmosphere (Mackay et al. 2010; Labrosse et al. 2010). Filaments and prominences are the same solar magnetic structures but appear distinctly due to their projection. Prominences, when observed on the disk, are known as solar filaments that lie along the polarity inversion line (Durrant 2002; Filippov & Srivastava 2011). Filaments may remain in the quiescent state for several days over the solar disk, while some filaments may exhibit eruptive nature. Filament eruption occurs mainly due to the non-equilibrium between the upward magnetic pressure and the downward magnetic tension, or due to the tether cutting between magnetic flux ropes containing filaments and overlaying arcades (Mackay et al. 2010). Filaments show different types of eruptions such as failed eruption (Liu et al. 2009), partial eruption (Tripathi et al. 2009), and full eruption (Schrijver et al. 2008; Chandra et al. 2010). Apart from these eruptions, filament can also undergo an asymmetric eruption with its one footpoint fixed in the photosphere (anchored leg) while the other participating in the dynamic motion (active leg) (Liu et al. 2009; Yang et al. 2012). Eruption of a flux rope can be partial or full that also depends on the overlying magnetic field configuration. Recently, Kumar et al. (2011) observed a huge flux-rope failed in the eruption, and found that the overlying filament remnant and coronal magnetic field caused its suppression. It is widely reported in the literatures that the emergence of new magnetic flux, generation of the high critical twist, low-lying atmospheric reconnections, can generate the eruptions and instability of the flux-ropes that may further lead to the outer coronal transients (Srivastava et al. 2010; Chandra et al. 2011; Yan et al. 2012; Zhang et al. 2012; Botha et al. 2012; Srivastava et al. 2013). However, it is also found that these conditions may only be the necessary conditions, which, may not be the sufficient conditions for the solar eruptions. The configuration of the ambient magnetic field as well as its strength may also play a role in deciding the nature

and morphology of the eruptions (Kumar et al. 2011, reference cited therein).

Eruptive filaments are closely associated with Coronal Mass Ejections (CMEs). CMEs are the propulsion of large-scale plasma and magnetic field into outer coronal and interplanetary space (Joshi et al. 2013). In general, a CME has a three part structure, i.e., a leading edge, dark cavity, and bright core associated with the eruptive filament (Riley et al. 2008, and reference therein). CMEs produce outward movement in the corona, and it may be either driven by the magnetic pressure or shock into the background of ambient solar wind (Filippov & Srivastava 2010). The less denser outer corona sometime shows downflows of the plasma blobs, CME cores, etc. Such downflows of the magneto-plasma are collectively termed as "coronal inflows" or "coronal downflows". Various kinds of downflows/inflows into the solar corona have been observed and analyzed, which include the prominence fall back (Tripathi et al. 2006, 2007), downflow over the post flare arcades (Innes et al. 2003; McKenzie & Hudson 1999; McKenzie 2000; Asai et al. 2004), inflow of small faint plasma structures and blobs, etc (Wang et al. 1999, 2000; Wang & Sheeley 2002; Sheeley & Wang 2002).

Innes et al. (2003) observed a series of dark, sunward moving flows, which were seen against the bright extreme ultraviolet post flare arcades of the large eruptive flare on 1999 April 21. Asai et al. (2004) examined the downflow motion above flare loops observed on 2002 July 23, and found that the plasma downflow occurred when the magnetic energy was released. In all these examples, the reconnection is responsible for the downflows in the inner solar corona. In spite of such observed downflows in the inner corona, reconnection in the outer corona may also be responsible for downflows there. Wang et al. (1999) reported various small and fainter plasma flows moving through the corona, and found that these inward motions are the observational signature of the gradual closing-down of magnetic flux-tubes dragged outward by the CMEs or other transient outflows. Wang et al. (2000)

studied the variety of small scale downflowing structures during the high solar activity (e.g., plasma blobs) and interpreted that these downflows were due to the magnetic reconnection between the closed and open field regions of the corona. Sheeley et al. (2001) reported that the inflow rate was dominated by transient bursts, which were correlated with the existence of non-polar coronal holes and other signatures of the solar non-axisymmetric open field structures. Wang & Sheeley (2002) and Sheeley & Wang (2002) identified faint, inward-moving features, e.g., collapsing loops, sinking plasma columns, falling plasma curtains, in and out pairs of oppositely directed plasma ejecta, and downflow of the core of CME at heliocentric distances from 2-6 R_{\odot} , and interpreted them as an initiation stage of the large-scale magnetic reconnection. Tripathi et al. (2006, 2007) also reported coronal downflows in the course of prominence eruption and associated coronal mass ejection on 2000 March 5, and interpreted that the origin of such downflows may be due to the reconnection inside the bifurcating flux-rope.

As said above, the CME core some time exhibits downfall depending upon the local magnetic field and plasma configurations, and the most probable reason may be the pre-settings of the large-scale reconnection in the outer corona. The CME itself can also produce several changes in the outer coronal magnetic fields in form of the deflection of coronal streamers, kink propagation in coronal rays, etc (Filippov & Srivastava 2010). Filippov & Srivastava (2010) analyzed the events of the interaction of CMEs with the coronal rays observed by SoHO/LASCO, and interpreted these deflections as the influence of magnetic field of a moving flux rope associated with the CME on the remote coronal rays. In the present paper, we report multi-wavelength investigation of asymmetric filament evolution and eruption, associated CME, coronal downflows, and their relationship using the observations from Solar Dynamic Observatory/Atmospheric Imaging Assembly (SDO/AIA), Solar Terrestrial Relation Observatory/Sun Earth Connection Coronal and Heliospheric Investigation (STEREO/SECCHI) and Solar and Heliospheric Observatory/Large Angle

and Spectrometer Coronagraph (SoHO/LASCO) C2 instruments on 2012 June 17-18 during 20:00–05:00 UT. The observational results are presented in Section 2. Physical scenarios of the observations are discussed in Section 3. Discussion and conclusions are outlined in the last section.

2. Observational Results

We use multi-wavelength and multi-instrument data from SDO/AIA (Lemen et al. 2012), STEREO-B/SECCHI (Wuelser et al. 2004), and SoHO/LASCO C2 coronagraph (Brueckner et al. 1995) for this study. We use SDO/AIA 304 Å and 171 Å data to study the filament evolution and its kinematics as it provides limb view for this event with less projection effect. SECCHI EUVI data (304 Å, 195 Å, and 171 Å) have been used to study the on-disk view of the filament evolution in the particular eruptive region. We also use LASCO C2 data to study the CME kinematics and the downflows of its core in the outer solar corona.

Fig. 1 shows the full disk images of the Sun in the STEREO/EUVI 171 Å and SDO/AIA 304 Å. The boxes in these images show the location of the filament. Observations from both the STEREO-B/SECCHI and SDO/AIA provide unique opportunity to study the filament eruption on the disk as well as on the limb respectively. The filament is located at the solar disk on the South-Western side as indicated by the box in the field of view of STEREO-B (Fig. 1, left image). On the same time, SDO/AIA observes the filament on the South-Eastern limb of the Sun (Fig. 1, right image). In the subsequent sections, we discuss the observations of the highly asymmetric filament eruption and the two-ribbon flare, as well as their association with the CME and the downflow of its core in the outer corona. Table 1 represents the time-line of the whole event started from the filament eruption, and end with the downflows of the CME core in the outer corona.

2.1. STEREO-B/SECCHI and SDO/AIA Observations of Asymmetric Filament Eruption and Two Ribbon Flare

Fig. 2 shows the sequence of selected EUV 304 Å images ($T_f = 0.07MK$) of the filament evolution as observed by STEREO-B/SECCHI. A long dark filament has been clearly seen on the South-West hemisphere over the solar disk (cf., snapshot at 20:26:36 UT). The leading edge (north-west part) of the eruptive filament is indicated by the white arrows. Thereafter, the whole filament exhibits whipping-like asymmetric eruption. A two ribbon flare was observed underneath the southern part of the former filament position. The flare was un-classified in the GOES X-ray fluxes because it occurred on the invisible side of the Sun. The two ribbons of the flare (indicated by R1 and R2 at the snapshot of 21:06:36 UT) are clearly visible. The flare occurred when the eruptive filament accelerated from slow speed to high speed (Fig. 7). For the detailed discussions of its physical scenario, we refer to the Section 3.1. The flare ribbons separate with each other along with the progress of the filament eruption. The north-western leg of the filament remains anchored on the Sun, while the whole material in the filament channel first whipped and later erupted asymmetrically. Fig. 3 shows the sequence of the selected EUV 195 Å ($T_f = 1.4MK$) images of the filament evolution observed by STEREO-B/SECCHI. The dark filament is also observed over the disk on the south-west of the solar disk (see the snapshot at 20:50:51 UT). In the coronal images, the fine and brightened coronal magnetic flux-tubes that cross the southern part of the filament, are clearly visible. The overlying magnetic field lines are clearly visible in this wavelength as indicated by the red arrows (cf., images at 21:00:51 and 21:05:52 UT in Fig. 3). These arches may be the part of a moderate active region lying on the eastern side of the filament (not shown here). The white arrows indicate the evolution of the leading edge (the north-west segment) of the filament in the corona. The two ribbon flare, and asymmetric whipping like eruption of the filament with its detached (southern) and anchored (northern) legs, are visible in 21:20:51 UT snapshot.

Fig. 4 and Fig. 5 respectively represent the sequence of the images in SDO/AIA 304 Å ($T_f = 0.05MK$) and 171Å ($T_f = 0.6MK$) channels showing the evolution of the filament eruption. The whole filament made-up of several threads is already visible on the south-east limb of the Sun on 2012 June 17. The white arrows indicate the leading edge of the eruptive filament. The observations show the asymmetric evolution and whipping of the filament (cf., filament.mpg). The whipping of the flux rope took place between $\approx 21:04$ and $\approx 21:10$ UT. During the whipping motion, most of the filament plasma channeled from the southern part to its northern part. The whipping and asymmetric eruption of the filament is indicated by the yellow arrow (cf., 21:10 UT snapshot in Figs. 4 and 5). After the whipping motion, the filament erupted asymmetrically higher in the corona towards the northern side of the Sun. The post flare loops in the southern side are visible during the decay phase of the flare (cf., 22:10:08 UT snapshot in Fig. 4 and 23:00 UT snapshot in Fig. 5). It is also interesting to note in the AIA 171 Å coronal image that the filament plasma shows some heating in the form of plasma brightening in the eruptive part. This may give a clue about the energy deposition and initiation of whipping-like asymmetric eruption through the magnetic reconnection in its southern part. This observational scenario matches well with the on-disk scenario of this filament eruption as observed by STEREO. The schematic representation of the asymmetric whipping like filament eruption and its comparison with SDO/AIA 304 Å image at 21:06:08 UT is shown in Fig. 6. The upper panel of Fig. 6 shows the SDO/AIA 304 Å image of the filament eruption at 21:06:08 UT. The arrows indicate the two legs of the filament. The filament image is rotated by 90 degree clockwise from its real position to compare with the schematic diagram. The bottom panel of Fig. 6 shows the schematic of the whipping like asymmetric filament eruption. Red line indicates the polarity inversion line.

Fig. 7 represents the height-time plot of the filament using the SDO/AIA 304 Å image sequence. The filament shows a slow rise followed by a fast rising phase. The speed of the

slow rise is around 3 km s^{-1} , while the fast rising phase has a speed of about $\approx 205 \text{ km s}^{-1}$. The filament rises slowly from 20:30 UT to 20:56 UT, and thereafter exhibits a fast rising phase from 21:00 UT to 21:14 UT. The whipping-like asymmetric eruption of the filament took place around its transition from the slow rise to the fast rise phase (Sterling & Moore 2005). After the whipping motion, the filament erupted with a high speed. The speed has been calculated from the linear fit to the height-time data. When we examine the composite image (Fig. 8) of the SoHO/LASCO white light image on 2012 June 17 at 23:24 UT and the SDO/AIA 304 Å image at 21:15 UT (inside), it shows occurrence of high degree of asymmetric filament eruption that later constitutes CME core. The detailed outer coronal dynamics is described in the next subsection.

2.2. LASCO C2 Observations of the CME and Downflow of Its Core in the Outer Corona

The LASCO C2 coronagraph observed the CME associated with the asymmetrical eruptive filament on 2012 June 17-18 during 21:36-04:48 UT. It was a slow CME and appears from the east side of the coronagraph occulting disk. Fig. 9 shows sequence of the difference images, showing the CME and its core eruption. Thereafter, the CME core falls down, which initiates the outer coronal downflows (cf., cme-downflow.avi). The CME first appears in the LASCO C2 field of view at $\approx 21:36$ UT on 2012 June 17. The red arrows in the panels (a)-(c) of Fig. 9, indicate the outward motion of the CME's leading edge. The core of the CME, which is the filament flux rope, was initially observed in the LASCO C2 field of view at $\approx 22:12$ UT. The position angle and the width of the CME were $\approx 90^\circ$ and $\approx 125^\circ$ respectively.

Fig. 10 shows the height-time plot of the CME leading edge, the CME core (Fig. 10a), and the derived velocity and acceleration profiles of the core with time (Fig. 10b), as well

as the same profiles with distance (Fig. 10c). The solid black line shows the linear fit of the form $y(t) = a + bt$ to the measured height of the CME leading edge w.r.t. time. From the linear fit, the speed ($dy(t)/dt = b$) of the CME leading edge is estimated as $\approx 540 \text{ km s}^{-1}$. The dotted blue line shows the height of the CME core w.r.t. time. From the linear fit to the upward motion of CME core, we obtain its average velocity as $\approx 126 \text{ km s}^{-1}$. Using the same method, we estimate the average velocity of $\approx 56 \text{ km s}^{-1}$ during the core downflow. In order to determine the velocity and acceleration at each point of the parabolic path of the CME core, we perform the third order fit. The blue dotted line over these points shows the third order fit of the form $y(t) = a + bt + ct^2 + dt^3$. The velocity and acceleration profiles are derived by differentiating the above equation at each point along the height-time profile (Fig. 10b). It is clear from Fig. 10b that the velocity of the CME core attains zero value at $\approx 00:48 \text{ UT}$ on 2012 June 18 when it reaches the maximum height. The CME core shows continuous deceleration. The deceleration rate changes from the initial value of -48 m s^{-2} to -19 m s^{-2} at the maximum height. Thereafter, it starts downflowing with acceleration rate from $\approx -21 \text{ m s}^{-2}$ at $00:48 \text{ UT}$ to $\approx 14 \text{ m s}^{-2}$ at $03:48 \text{ UT}$ (cf., velocity and acceleration profiles in Fig. 10b). We also plot the velocity and acceleration profiles of the CME core w.r.t. radial distance. The initial velocity at $\approx 2.54 R_{\odot}$ is $\approx 312 \text{ km s}^{-1}$, which continuously decreases with height and becomes zero at $\approx 4.33 R_{\odot}$ (cf., Fig. 10c). After the start of downflow from $\approx 4.33 R_{\odot}$, its initial speed is around $\approx 10 \text{ km s}^{-1}$ that later reaches up to $\approx 30 \text{ km s}^{-1}$ at $3.56 R_{\odot}$. The initial deceleration was $\approx 48 \text{ m s}^{-2}$ at the height of $\approx 2.54 R_{\odot}$. At $4.33 R_{\odot}$, the deceleration was 21 m s^{-2} , while during the fall of the core from this height, it reaches to zero and then tends towards positive values. The value of deceleration/acceleration during the motion of the core was not matching to the local gravitational acceleration $GM_{\odot}/r^2 \sim 68(2R_{\odot}/r)^2 \text{ m/s}^2$ (Wang & Sheeley 2002) (cf. Fig. 10c). This evidently shows that the gravity is not the dominant factor for the observed downward motion. We also observe the interaction of the CME with the coronal ray in

the northward direction of the outward moving core. The red curve in the Fig. 10a shows the coronal ray deflection from its mean position at a height of $\approx 3.1 R_{\odot}$. The deflection started around 22:12 UT on 2012 June 17 soon after the appearance of CME core in the LASCO field of view and continued with the upward motion of the CME. The coronal ray is deflected maximum of 3.2×10^5 km at $\approx 22:36$ UT in the north and then returns back to its mean position.

3. Physical Scenario of the Observed Dynamics

The observations of the asymmetric filament eruption, formation of the two ribbon flare, and their relationship with the CME and the outer coronal downflows are discussed in detail in the previous section. In the present section, we describe the possible physical scenarios and theoretical interpretations for the observed coronal dynamics.

3.1. Asymmetric Filament Eruption and Two Ribbon Flare

The asymmetric flux-rope eruptions are studied by various authors (Tripathi et al. 2006; Liu et al. 2009, and reference therein). We observed the whipping-like asymmetric filament eruption. The whipping like asymmetric filament eruption is characterized when active leg whips upward, and hard X-ray sources shift toward the end of the anchored leg (Liu et al. 2009). We do not have the X-ray observations in our case. However, we could not find any evidence of the transport of flare ribbon brightening (low energy counterparts) towards the anchored leg of the filament. This is some what unique situation differing from the observations of Liu et al. (2009). In the present observational base-line, it is clear that the northern part of the filament has comparatively homogeneous overlying corona, while its southern part experienced the crossing overlying thin and brightened flux-tubes.

In the south-east direction of it, there was a moderate active region whose arches were crossing above the southward part of the filament and made it initially suppressed. During the whipping motion of the southern part of filament these overlaying magnetic flux-tubes probably allow only the formation of a compact two ribbon flare beneath the eruptive part of the filament. This flare brightness does not spread much along the neutral line as in the case of large flares (Benz 2008).

The filament erupts asymmetrically and the two ribbon flare occurs beneath of it. The flare may be triggered due to reconnection in the vertical current sheet between surrounding coronal fields in the wake of the eruptive filament (Carmichael 1964; Sturrock 1966; Hirayama 1974; Kopp & Pneuman 1976; Shibata 1999, reference cited therein). As the reconnection progresses as per those canonical models, formation of post-flare loops, propagation of the brightening along the ribbons as well as their separation are evident in the lower part of the solar atmosphere.

3.2. The coronal Downflows due to the Flux-rope Failed Eruption.

The eruptive filament further leads to a CME whose core is constituted by it. The degree of asymmetry in this eruption is large. It is clear from the Fig. 8 that inspite of radial motion, the filament expands in the outer corona (CME core) almost at an angle of $\approx 50^\circ$ and constitutes the outer coronal dynamics in form of downflow. The core later on shows the downflow of its plasma. The physical reason in the present observational base-line may be two-fold, e.g., (i) The self-consistent equilibrium of the flux-rope below a critical height, during its subsequent eruption in form of whipping motion and formation of the CME's core (Filippov et al. 2001, 2002). (ii) The interaction of the moving CME core with the ambient medium that drags out its momentum (Wang & Sheeley 2002). Before the start of downflow, CME core causes the deflection of a coronal ray in the northward

direction in the LASCO C2 field-of-view (cf. Fig. 9). The deflection measurement has been carried out at a height of around $\approx 3.1 R_{\odot}$. The ray started deflecting around 22:12 UT and reaches up to a maximum displacement of 3.2×10^5 km at $\approx 22:36$ UT on 2012 June 17 (cf., Fig. 10a). This was the period when CME core was trying to move ahead with the average velocity of ≈ 126 km s $^{-1}$ (cf., Fig. 10b). The coronal ray deflection and its re-storing may be most likely caused by the expansion of the CME-core magnetic field and its interaction with the radial field of the coronal ray (Filippov & Srivastava 2010). However, during the coronal ray restoring motion, the downflow of CME core starts when the coronal ray moved almost 50% towards its equilibrium position on $\approx 01:00$ at 18 June 2012 (cf. Figs. 9 and 10a). This was the time when CME core starts down flowing with an average speed of around 56 km s $^{-1}$. Both the southward opposite motion of coronal ray (in projection), and coronal downflow, were progressed simultaneously later on, and finally ended at $\approx 03:48$ UT on 2012 June 18. This interaction and co-temporal dynamics of the coronal ray and coronal downflow is, to the best of our knowledge, observed for the first time in the presented observations. However, the one-to-one relation between the coronal ray restoring and downflow is not established here as the downflow starts after two hour from the initiation of restoring motion of the deflected coronal ray towards its equilibrium position. Therefore coronal ray deflection may be only the consequence of the upward moving CME, however, it does not start the downflow of CME core.

The most likely cause may be the self-consistent evolution of the flux-rope itself, which forms the CME core. We compare the observed evolution of the eruptive filament and CME with the model developed by Filippov et al. (2001, 2002) for the non-radial flux-rope motion previously. It was applied to the event on 1997 December 14 whose initial phase was very similar to the eruption studied in the present paper. In the December 14 event, the filament erupted from middle latitude in the southern hemisphere, while the CME was observed close to the equatorial plane. In the present case, the CME core propagates even

at some angle to the north of the equatorial plane (cf. Fig. 8). In both cases, the filaments passed significant distances along the latitude direction. However on 1997 December 14, the true fast CME was observed, while in the present case, on 2012 June 17-18, the CME core is stopped at some height and then fall down.

In the axially-symmetric model of Filippov et al. (2001, 2002), the flux-rope was represented by a thin current-carrying plasma ring (torus) with a total electric current I located above the photosphere along a heliographic parallel. A similar model for a ring located in the equatorial plane was analyzed by Lin et al. (1998). After integrating over the torus volume, we can obtain the equation of motion of the torus as a whole, as well as an equation describing variation of its inner radius. In cylindrical coordinates (ρ, φ, z) with their origin at the solar center and the z axis directed along the rotational axis, the equations of motion for a toroidal segment with unit length take the form

$$m \frac{d^2 \rho}{dt^2} = \frac{I}{c} (B_z^{(ex)} + B_z^{(m)} + B_z^{(I)}) - mgR^2 \frac{\rho}{(\rho^2 + z^2)^{3/2}} - kv_p, \quad (1)$$

$$m \frac{d^2 z}{dt^2} = -\frac{I}{c} (B_\rho^{(ex)} + B_\rho^{(m)}) - mgR^2 \frac{z}{(\rho^2 + z^2)^{3/2}} - kv_z, \quad (2)$$

where m is the mass of the filament per unit length, $B^{(ex)}$ is the magnetic field produced by sources located beneath the photosphere and by currents in the solar-wind region, $B^{(m)}$ is the field produced by inductive currents in the photosphere that prevents the penetration of the coronal-current field into the Sun, $B^{(I)}$ is the field produced by the current flowing along the ring axis, g is the free-fall acceleration at the photospheric level, k is the dissipation coefficient, and v is the velocity.

We used the same parameters of the model as in Filippov et al. (2002) except the mass of the filament per unit length. It was chosen as 10^5 g cm^{-1} , a more typical value

for an average filament, because we do not need to fit the result to the final velocity of 500 km s^{-1} . The global coronal field $B^{(ex)}$ is represented by two spherical harmonics, dipole and octupole. These harmonics dominate in the global field in the epoch of solar activity minimum. Our event does not occur at minimum, however, the level of activity in June 2012 was not very high as the monthly averaged sunspot number was about 60, thus the global magnetic field configuration was not typical for the maximum. The harmonic coefficients are chosen in such a way that the magnetic field strength is $B \approx 1 \text{ G}$ in the corona near the filament, and there is a null line at the height of $0.2 R_{\odot}$ above the equator. In this field, a flux rope with the current of $\approx 10^{11} \text{ A}$ will be in equilibrium at the height of $\approx 30 \text{ Mm}$. The equilibrium is defined mainly by the components of the Lorentz force in Equations (1) and (2). The gravity force is about two orders of magnitude weaker than the electromagnetic forces acting on the filament. It does not appreciably affect the equilibrium position in the lower corona, however the filament mass is significant for the kinematics of eruption.

Each value of the current corresponds to two equilibrium points in this curve - one above and one below some critical point whose current I_c corresponds to a single solution of Equations (1) and (2) with zero left-hand terms. If the current exceeds the critical value, equilibrium cannot be achieved in the corona. The left panels of Fig. 11 shows the evolution of the flux rope without dissipation after the loss of equilibrium due to the increase of the electric current strength on a small value (about 2%) over the critical value. We see that the true flux rope eruption started in the southern hemisphere and propagating into the northern hemisphere.

It was pointed out by Filippov et al. (2001) that there is a stable equilibrium position higher in the corona for the erupting flux rope, but the gained kinetic energy of the flux rope does not allow it to stop in the higher equilibrium position. However, if we add

some dissipation $-kv$ to the right hand side of the equations of motion, as it was done by Filippov et al. (2001) for testing of the initial equilibrium stability, the flux rope can lose its momentum and stop at some height (the right panels of Fig. 11). We choose the value of k as $2 \times 10^2 \text{ g sec}^{-1}$ in order to stop the ascending motion of the flux rope at the height of $4 R_{\odot}$. At the speed of 300 km s^{-1} , it creates the drag force $kv = 6 \times 10^9$ dyne per unit length or about an order of magnitude stronger than the gravitational force $fg = 7 \times 10^8$ dyne at the height of $2 R_{\odot}$. Although we did not apply additional efforts to fit to the observational data, we can see that the kinematics shown in the right panels of Fig. 11 is very similar to the observed kinematics presented in Fig. 10. We compare the segments of curves between the dashed vertical lines in Fig. 11d with the dotted blue line fitting in Fig. 10a and the segments of curves between the dashed vertical lines in Fig. 11e with the black dotted line connecting the data points in Fig. 10b. They show 6-hours interval of the CME core evolution. Evidently, the curves are very similar and the quantities are close to each other. Comparison of Fig. 8 with the calculated trajectory in Fig. 11f also confirms the conclusion that the model rather adequately describes the observed event. However, the nature of the dissipation or the drag force is unclear for us. Possibly it is the aerodynamic drag or includes some additional dissipative mechanisms.

4. Discussion and Conclusions

We have presented the multi-wavelength analysis and the relationship of whipping-like asymmetric filament eruption, the associated CME, and the outer coronal downflows in the form of CME core on 2012 June 17-18. The summary of the obtained results of this study is as follows:

1. The observation shows a whipping like highly asymmetric filament eruption with

active (south-eastern) leg and the anchored (north-western) leg.

2. During the eruption, a two ribbon flare occurred underneath the eastern part of the filament. This supports well the standard flare model (CSHKP) of reconnection.
3. The deceleration profile of the CME core shows that the gravity is not only the force responsible for the downflow. The downflow of the CME core has been observed which may be due to the self consistent evolution of the flux-rope in the coronal magnetic field.
4. Coronal ray deflection occurs during the upward motion of the CME, however, it does not reveal exact correlation with the coronal downflows.

Recently Liu et al. (2009) presented observation of two types of asymmetric filament eruptions, i.e., whipping and zipping like configurations. In the whipping like eruptions, active leg whips upward, and the observed hard X-ray source locations shift towards the anchored leg. While in the zipping like asymmetric eruption, active leg moves along the neutral line and the hard X-ray sources move away from the anchored leg. In our present observations, the filament eruption is whipping-type highly asymmetric eruption, however, without any significant propagation of flare brightening towards its anchored leg. Whipped filament also rises from nearby its southern activated footpoint, and energy deposition in the form of flare ribbons occurred only beneath of it. The asymmetric eruption of the filament later produced a slow CME that deflects the coronal ray in the outer corona. Thereafter, the coronal downflow is observed from $\approx 4.33 R_{\odot}$ towards the Sun. Previously, Wang & Sheeley (2002), observed the CME core fallback during 1998-2001. They found that the fallback events occur in impulsive but relatively slow CMEs. The fall down of core material may be due to its interaction with the background plasma which removes the momentum of the CME core. McKenzie & Hudson (1999) observed a downward flow above the coronal arcades during the decay phase of solar flare on 1999 January 20, and interpreted it as cross sections of evacuated flux-tubes resulting from the intermittent reconnection following the

associated CME. However, in the present case, we have a moderate CME beyond $2 R_{\odot}$ with its core, formed by highly asymmetric filament eruption that may start downflowing due to its self-consistent evolution in the coronal magnetic field as shown in our model calculations (Fig. 11).

In conclusion, our present multiwavelength study provides a unique relationship between the asymmetric filament eruption, flare as per standard model, associated CME, and the initiation of coronal downflows around $\approx 4.33 R_{\odot}$. Such studies may have important implications on the physical conditions of the outer corona and its coupling through various types of transients and plasma dynamics occurred in the lower solar atmosphere. New observations should be performed using future high-resolution observations from space and ground to shed new light on such significant phenomena and their relationship in the solar atmosphere.

We thank anonymous referee for his/her valuable comments and suggestions. The authors thank Indo-Russian (DST-RFBR) Project on "Study of Dynamical Events in the Solar Atmosphere during Maximum of Solar Cycle 24 (INT/RFBR/P-117 RFBR 12-02-00008 and 12-02-92692)" for its support to this study during our bilateral collaboration. NCJ thanks Aryabhata Research Institute of Observational Sciences (ARIES), Nainital for providing Post Doctoral Grant. BF was supported in part also by the Program # 22 of the Russian Academy of Sciences. We also acknowledge partly the support of IUSSTF/JC-Solar Eruptive Phenomena/99-2010/2011-2012 project. AKS thanks Shobhna Srivastava for the patient encouragements for his research works.

REFERENCES

- Asai, A., Yokoyama, T., Shimojo, M., & Shibata, K. 2004, *ApJ*, 605, L77
- Benz, A. O. 2008, *Living Reviews in Solar Physics*, 5, 1
- Botha, G. J. J., Arber, T. D., & Srivastava, A. K. 2012, *ApJ*, 745, 53
- Brueckner, G. E., Howard, R. A., Koomen, M. J., et al. 1995, *Sol. Phys.*, 162, 357
- Carmichael, H. 1964, *NASA Special Publication*, 50, 451
- Chandra, R., Pariat, E., Schmieder, B., Mandrini, C. H., & Uddin, W. 2010, *Sol. Phys.*, 261, 127
- Chandra, R., Schmieder, B., Mandrini, C. H., et al. 2011, *Sol. Phys.*, 269, 83
- Durrant, C. J. 2002, *Sol. Phys.*, 211, 83
- Filippov, B., & Srivastava, A. K. 2010, *Sol. Phys.*, 266, 123
- Filippov, B., & Srivastava, A. K. 2011, *Sol. Phys.*, 270, 151
- Filippov, B. P., Gopalswamy, N., & Lozhechkin, A. V. 2001, *Sol. Phys.*, 203, 119
- Filippov, B. P., Gopalswamy, N., & Lozhechkin, A. V. 2002, *Astronomy Reports*, 46, 417
- Hirayama, T. 1974, *Sol. Phys.*, 34, 323
- Innes, D. E., McKenzie, D. E., & Wang, T. 2003, *Sol. Phys.*, 217, 247
- Joshi, N. C., Uddin, W., Srivastava, A. K., et al. 2013, [arXiv:1303.1251](https://arxiv.org/abs/1303.1251)
- Kopp, R. A., & Pneuman, G. W. 1976, *Sol. Phys.*, 50, 85
- Kumar, P., Srivastava, A. K., Filippov, B., Erdélyi, R., & Uddin, W. 2011, *Sol. Phys.*, 272, 301

- Labrosse, N., Heinzl, P., Vial, J.-C., et al. 2010, *Space Sci. Rev.*, 151, 243
- Lemen, J. R., Title, A. M., Akin, D. J., et al. 2012, *Sol. Phys.*, 275, 17
- Lin, J., Forbes, T. G., Isenberg, P. A., & Demoulin, P. 1998, *ApJ*, 504, 1006
- Liu, R., Alexander, D., & Gilbert, H. R. 2009, *ApJ*, 691, 1079
- Mackay, D. H., Karpen, J. T., Ballester, J. L., Schmieder, B., & Aulanier, G. 2010, *Space Sci. Rev.*, 151, 333
- McKenzie, D. E. 2000, *Sol. Phys.*, 195, 381
- McKenzie, D. E., & Hudson, H. S. 1999, *ApJ*, 519, L93
- Riley, P., Lionello, R., Mikić, Z., & Linker, J. 2008, *ApJ*, 672, 1221
- Schrijver, C. J., Elmore, C., Kliem, B., Török, T., & Title, A. M. 2008, *ApJ*, 674, 586
- Sheeley, N. R., Jr., Knudson, T. N., & Wang, Y.-M. 2001, *ApJ*, 546, L131
- Sheeley, N. R., Jr., & Wang, Y.-M. 2002, *ApJ*, 579, 874
- Shibata, K. 1999, *Ap&SS*, 264, 129
- Srivastava, A. K., Erdélyi, R., Tripathi, D., et al. 2013, *ApJ*, 765, L42
- Srivastava, A. K., Zaqarashvili, T. V., Kumar, P., & Khodachenko, M. L. 2010, *ApJ*, 715, 292
- Sterling, A. C., & Moore, R. L. 2005, *ApJ*, 630, 1148
- Sturrock, P. A. 1966, *Nature*, 211, 695
- Tripathi, D., Gibson, S. E., Qiu, J., et al. 2009, *A&A*, 498, 295

- Tripathi, D., Isobe, H., & Mason, H. E. 2006, *A&A*, 453, 1111
- Tripathi, D., Solanki, S. K., Mason, H. E., & Webb, D. F. 2007, *A&A*, 472, 633
- Tripathi, D., Solanki, S. K., Schwenn, R., et al. 2006, *A&A*, 449, 369
- Wang, Y.-M., Sheeley, N. R., Jr., Howard, R. A., Cyr, O. C. S., & Simnett, G. M. 1999, *Geophys. Res. Lett.*, 26, 1203
- Wang, Y.-M., Sheeley, N. R., Socker, D. G., Howard, R. A., & Rich, N. B. 2000, *J. Geophys. Res.*, 105, 25133
- Wang, Y.-M., & Sheeley, N. R., Jr. 2002, *ApJ*, 567, 1211
- Wuelser, J.-P., Lemen, J. R., Tarbell, T. D., et al. 2004, *Proc. SPIE*, 5171, 111
- Yan, X. L., Qu, Z. Q., & Kong, D. F. 2012, *AJ*, 143, 56
- Yang, J., Jiang, Y., Yang, B., et al. 2012, *Sol. Phys.*, 279, 115
- Zhang, J., Cheng, X., & Ding, M.-D. 2012, *Nature Communications*, 3,

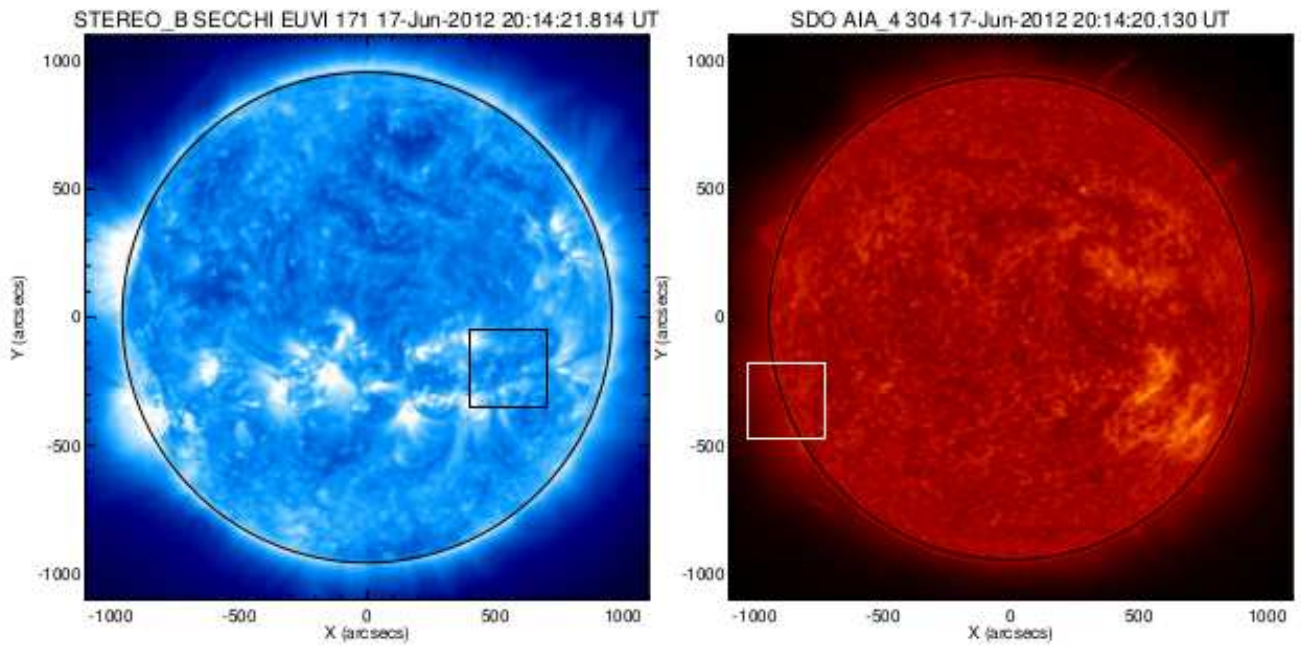


Fig. 1.— STEREO-B/SECCHI 171 Å (left) and SDO/AIA 304 Å (right) images showing the full disk of the Sun on 2012 June 17. The boxes show the location of the filament from two different angles.

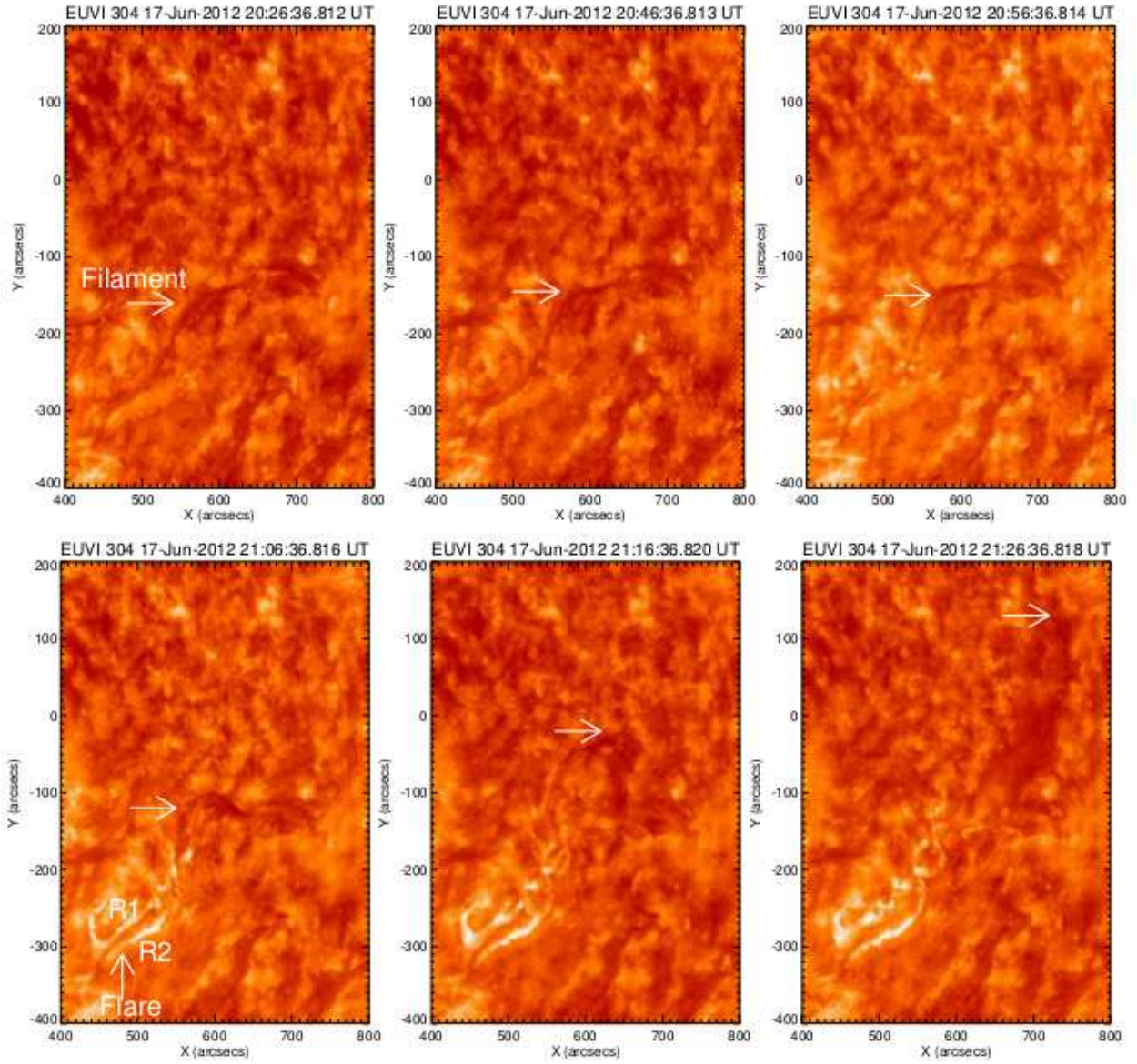


Fig. 2.— STEREO B/SECCHI 304 Å images showing the activation and eruption of the filament and the triggering of a two ribbon flare near the South-Eastern foot point. The two ribbons of the flare are represented by R1 and R2.

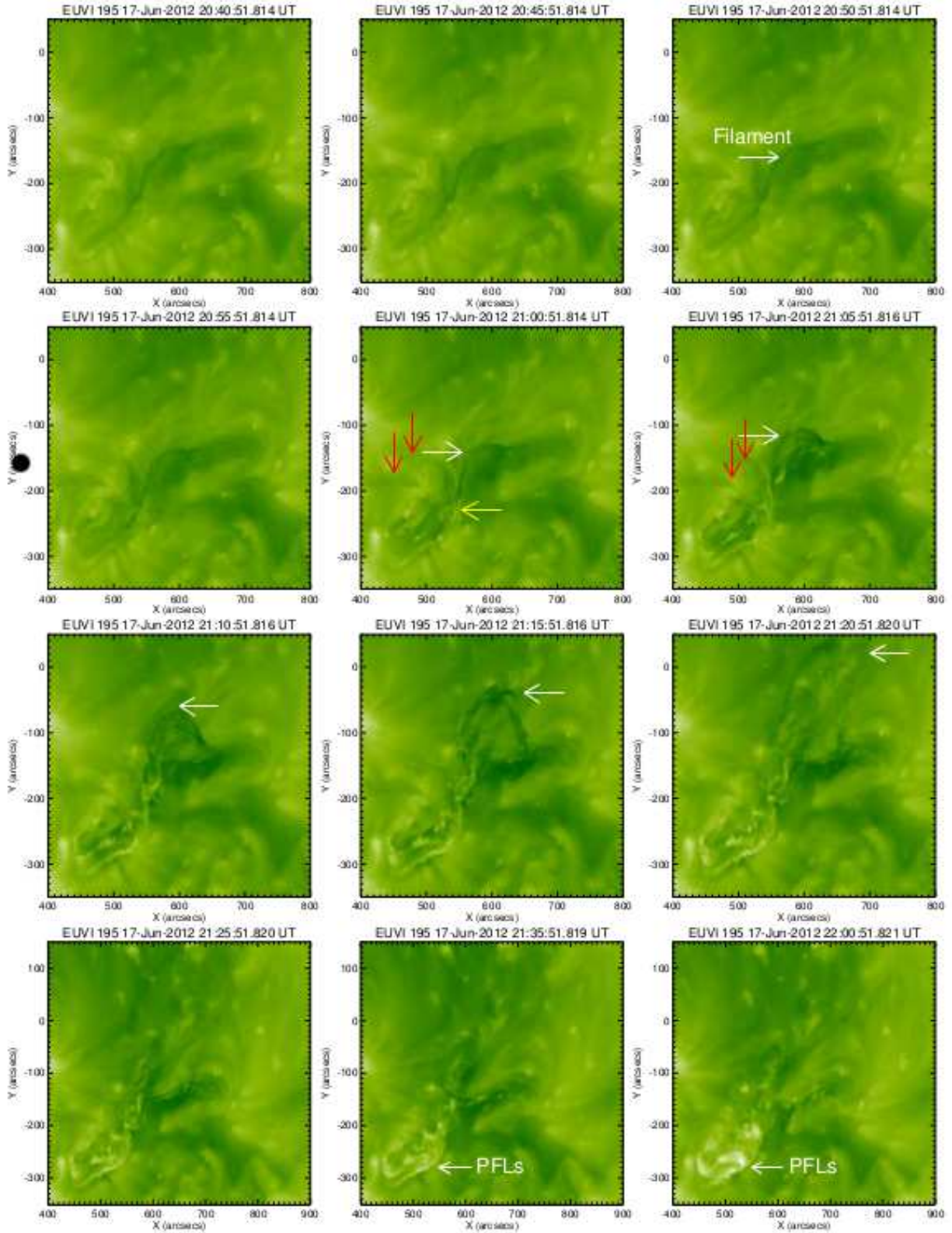


Fig. 3.— STEREO-B/SECCHI 195 Å images showing the activation of the filament. The white arrows represent the eruption of the filament. Downward red arrows indicate the overlaying magnetic field arches above the southern part of the filament. The yellow arrow indicates the interaction of filament with the overlaying magnetic field. Post flare loops (PFLs) are presented in the bottom panel.

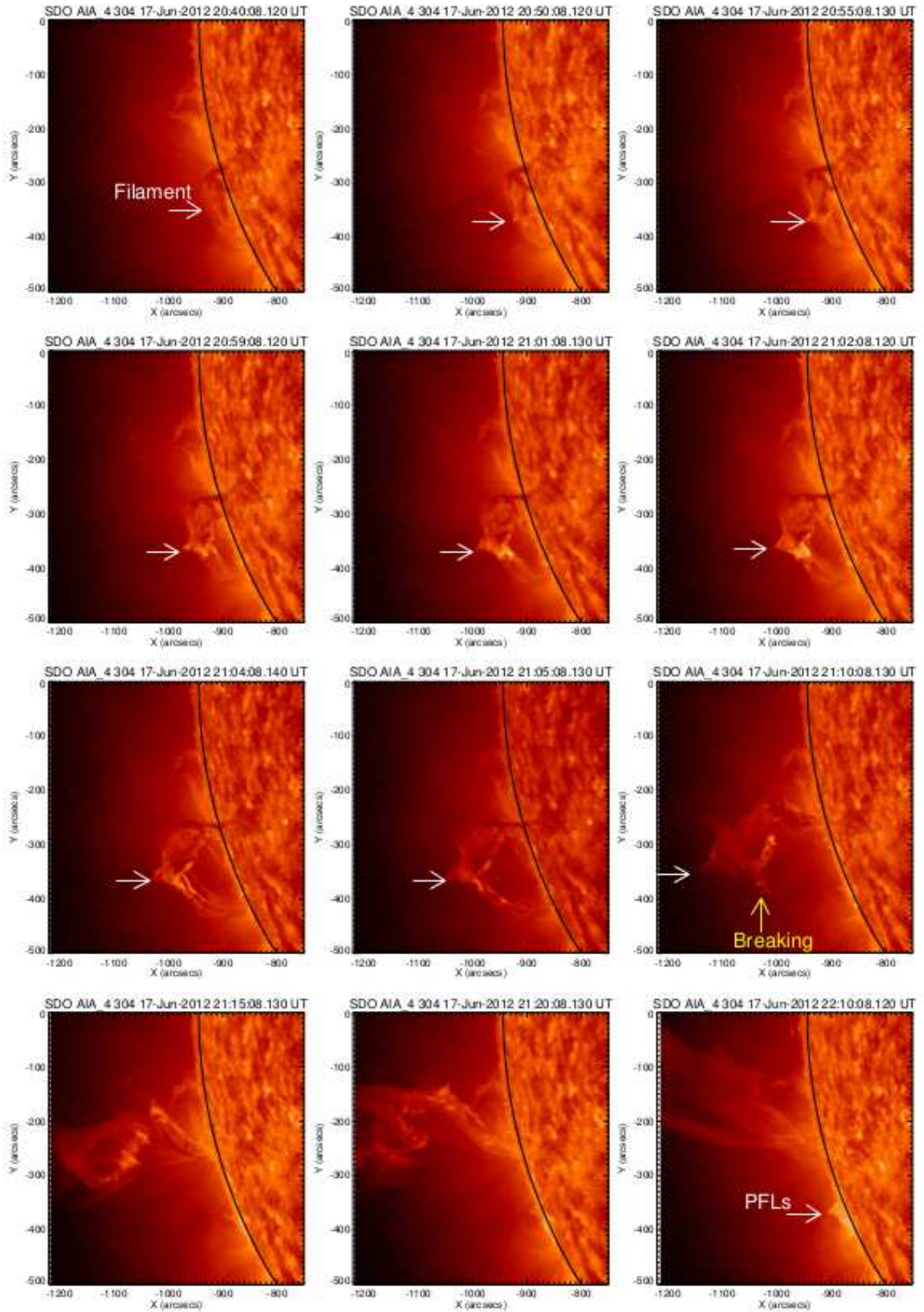


Fig. 4.— SDO/AIA 304 Å images showing the evolution and eruption of the filament. White arrows indicate the erupting leading edge of the filament. The bottom right corner image

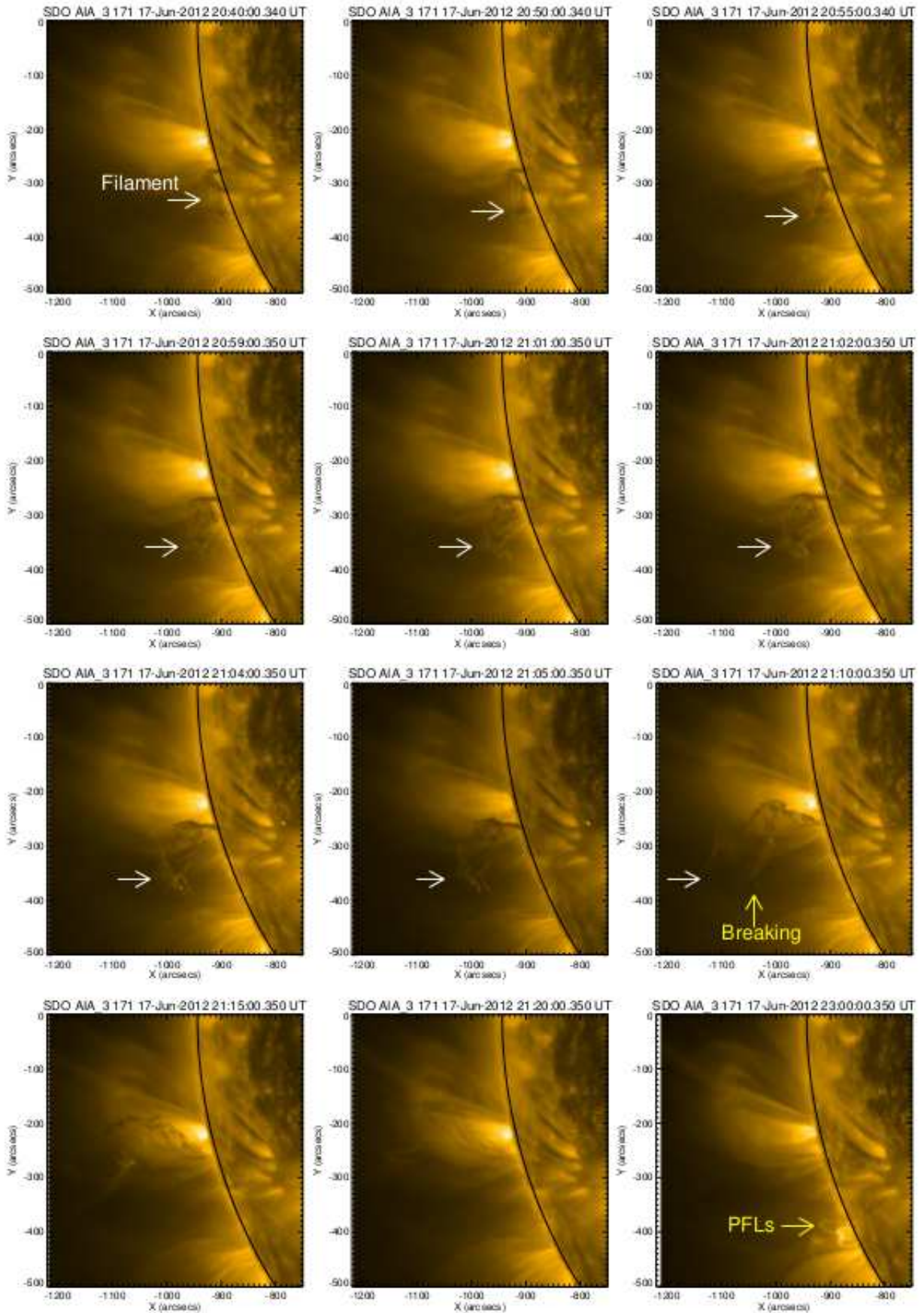


Fig. 5.— SDO/AIA 171 Å images showing the evolution and eruption of the filament. White arrows represent the evolution of the filament leading edge. Post flare loops (PFLs) on the

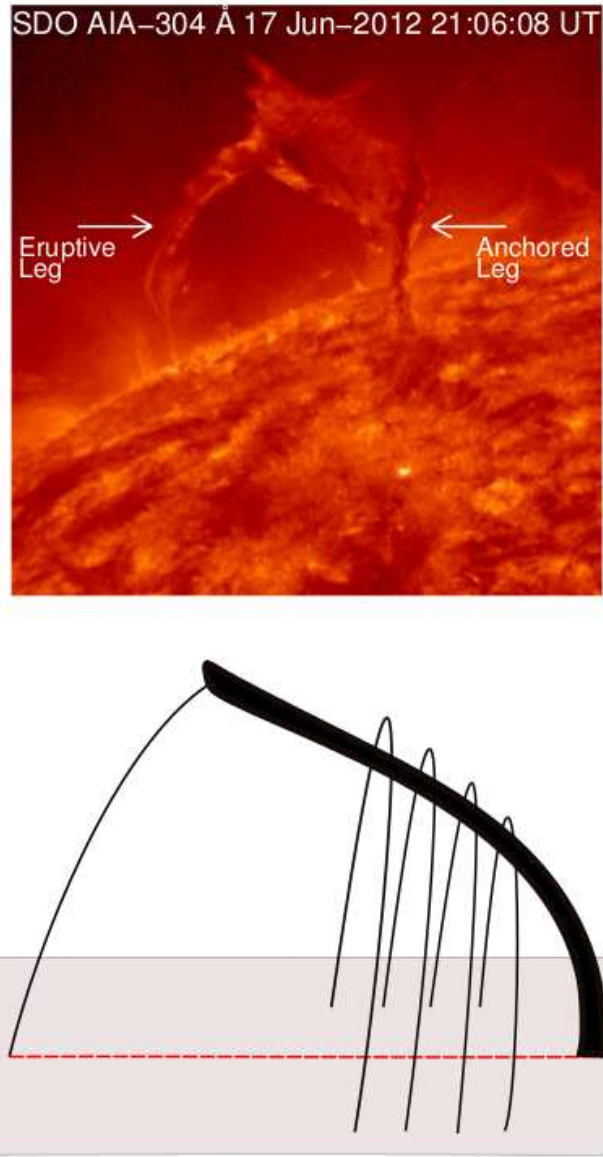


Fig. 6.— Upper panel: SDO/AIA 304 Å image of the filament eruption at 21:06:08 UT. The arrows indicate the two legs of the filament. The filament image is rotated by 90 degree clockwise from its real position just to compare with the schematic diagram. Bottom panel: Schematic diagram of the whipping like asymmetric filament eruption. Red line indicates the polarity inversion line.

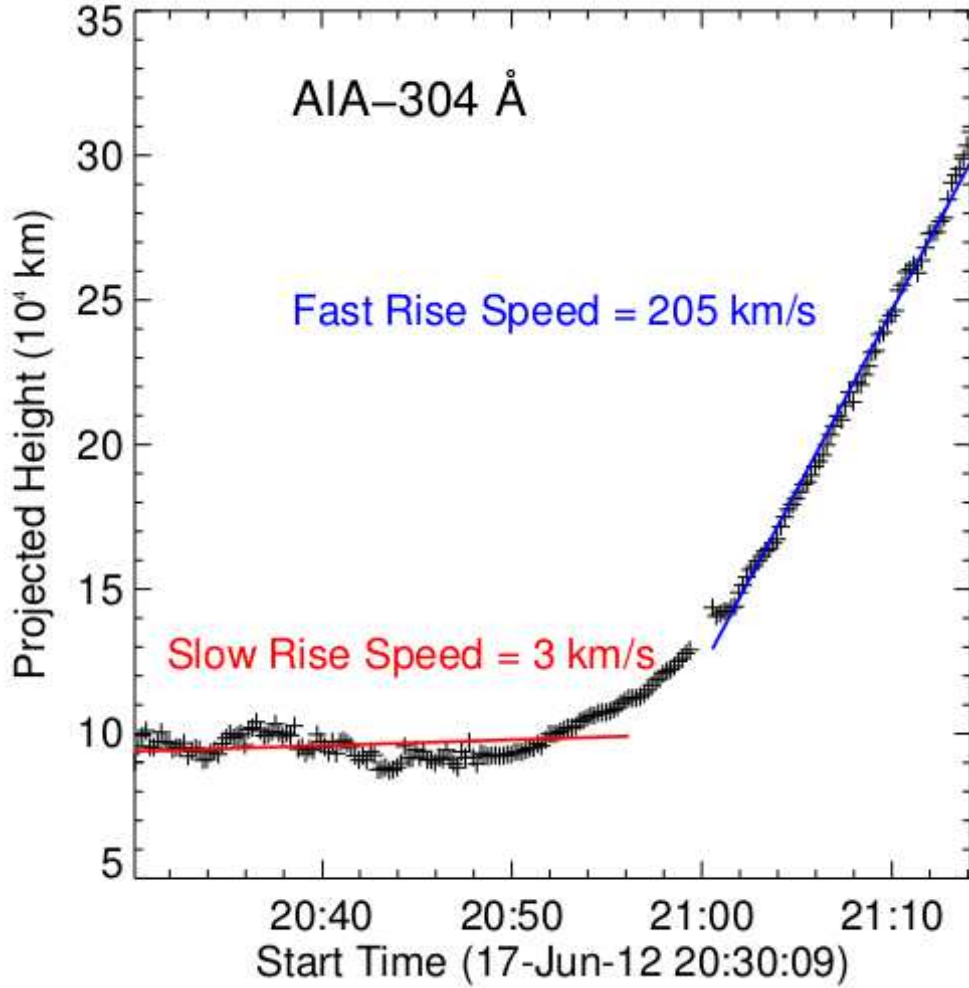


Fig. 7.— Height-time plot of the filament leading edge (indicated by the white arrows in the Fig. 4) measured using SDO/AIA 304 Å time-series.

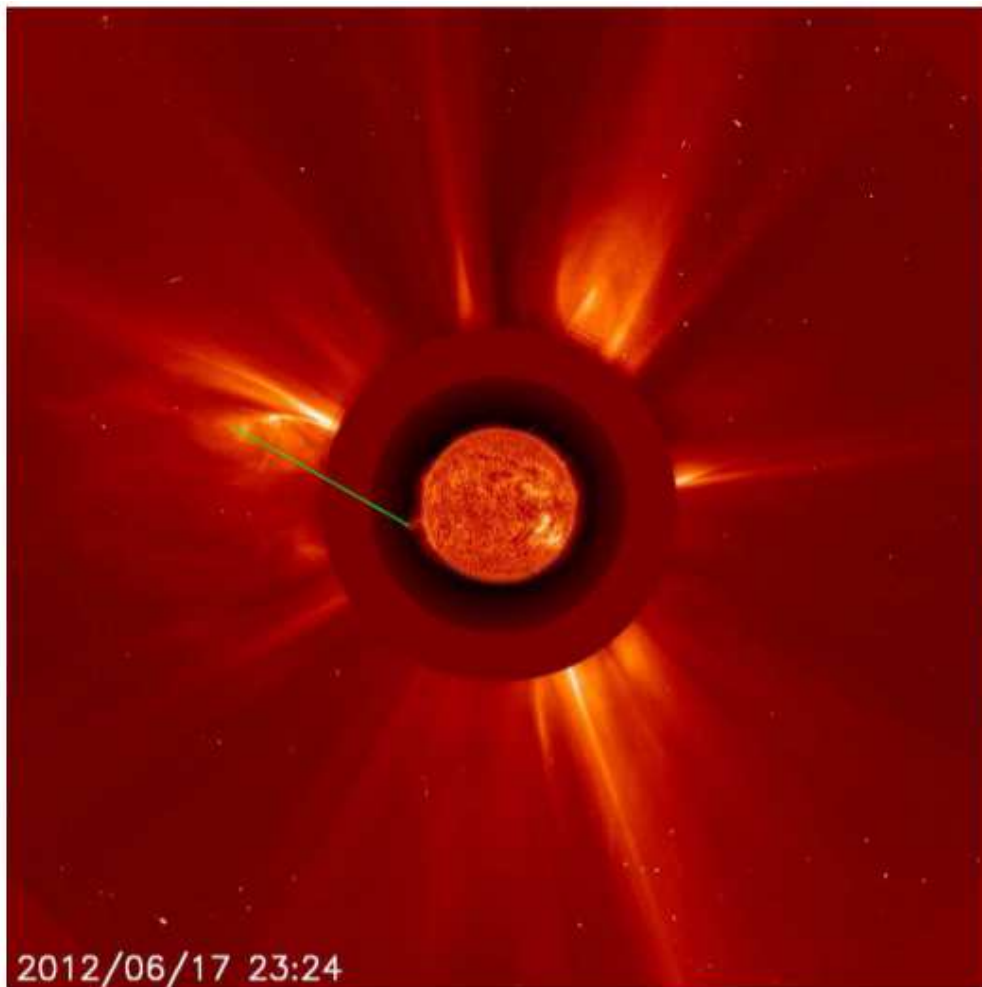


Fig. 8.— Composite image of the white-light SOHO/LASCO-C2 image on 2012 June 17 at 23:24 UT and SDO/AIA 304 Å image at 21:15 UT (inside). Green line shows the approximate trajectory of the eruptive prominence.

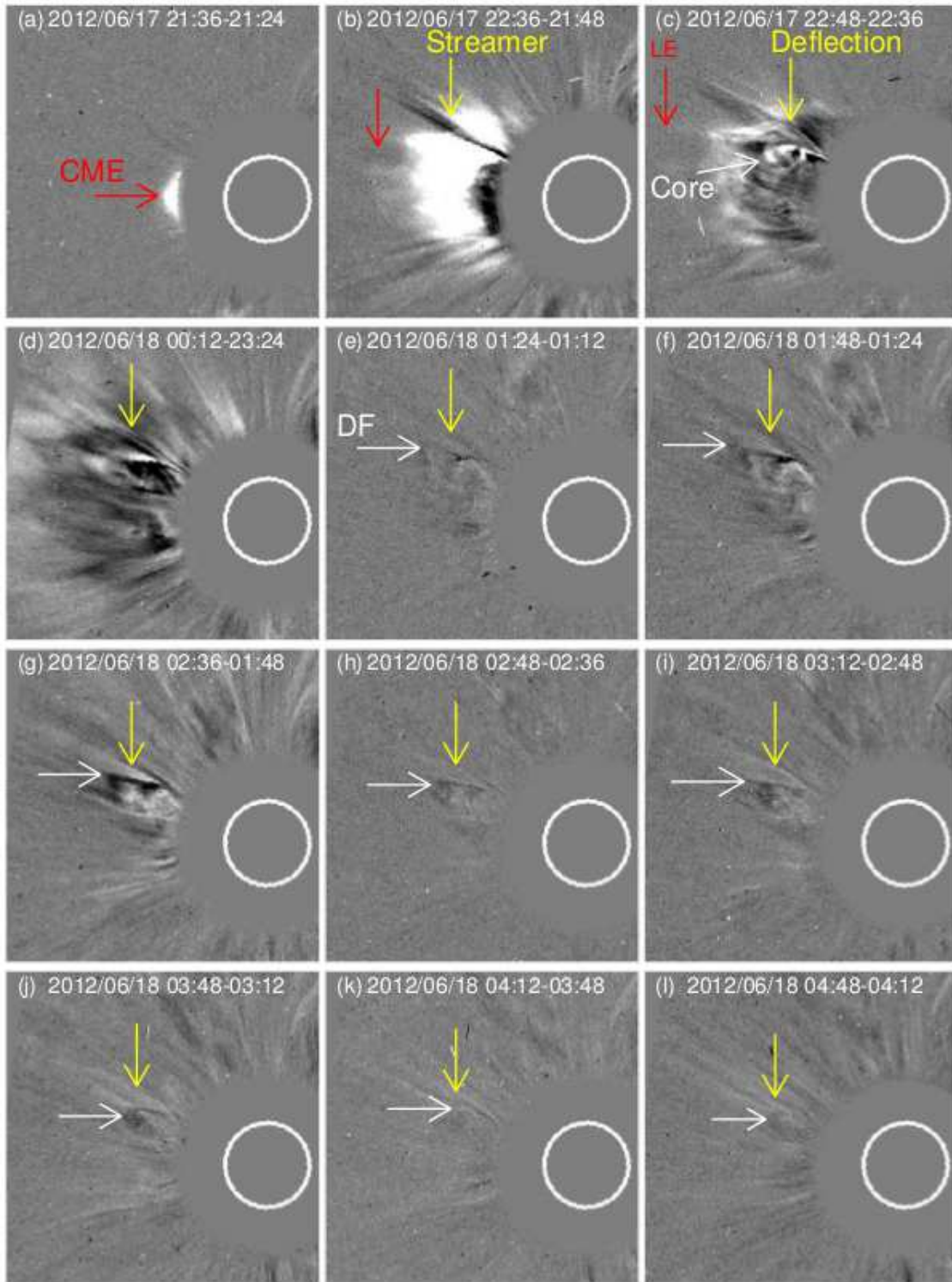


Fig. 9.— Time sequence of LASCO C2 images showing the CME eruption (a-d) and falling down of the CME core material (e-l) on 2012 June 17-18. Red arrows indicate the evolution of the CME leading edge (LE). White arrows indicate the down flow (DF) of the CME core. Yellow arrows indicate the coronal ray deflection. These difference images have been taken

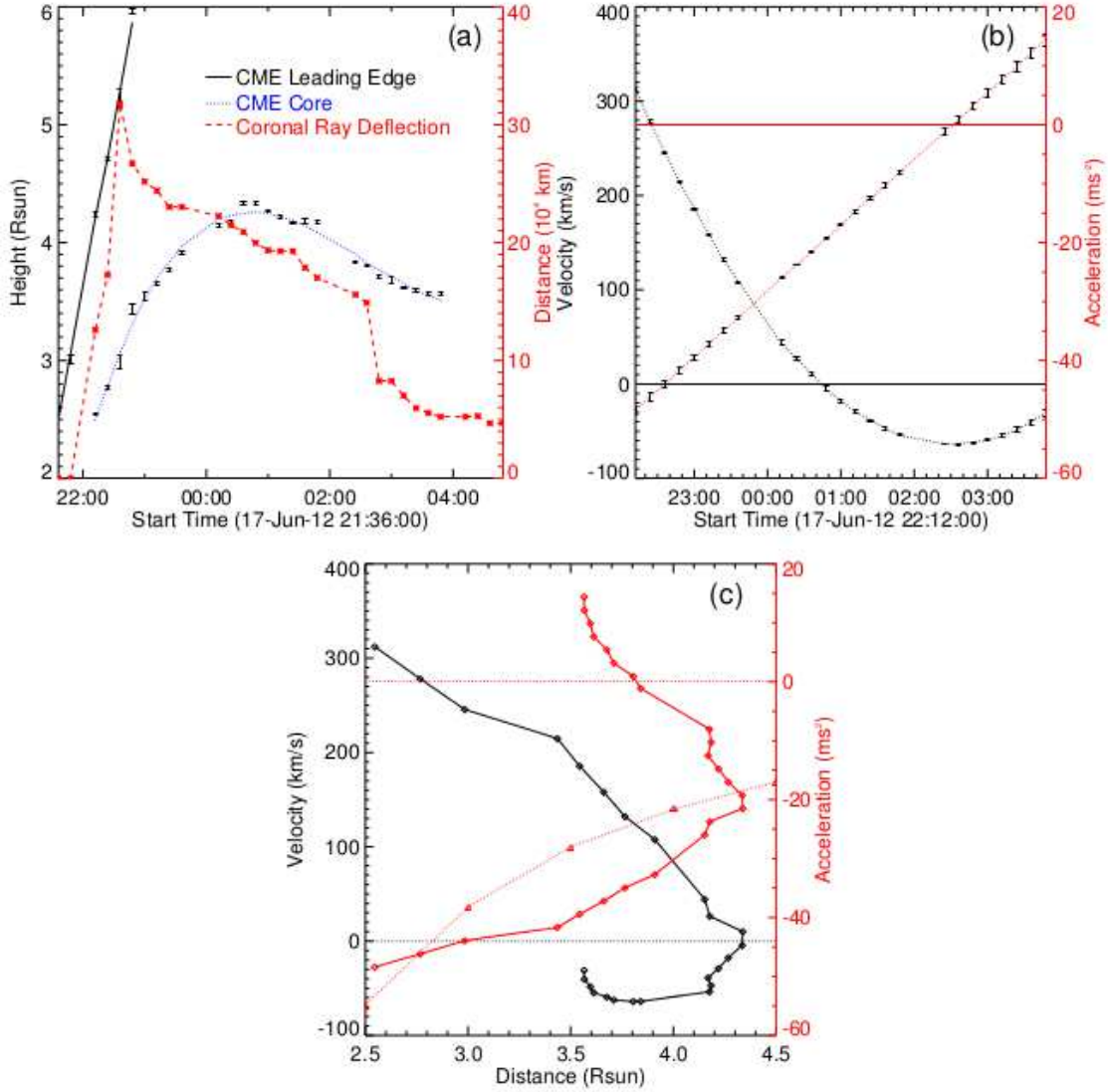


Fig. 10.— (a) Height-time plot of the CME core and leading edge. The solid black line represents the linear fit to the CME leading edge data. The dotted blue curve in this figure represents the third order fit to the core height-time data. (b) Speed-time and acceleration-time plots of the CME core. Error bars in the panel (a-c) are the standard deviation computed from the three repeated measurements. (c) Distance-velocity and distance-acceleration plots of the CME core. The velocity and acceleration are represented by the black and red colors respectively. The red dotted curve with triangle symbols in the panel (c) corresponds to the local gravitational acceleration $-GM_{\odot}/r^2$.

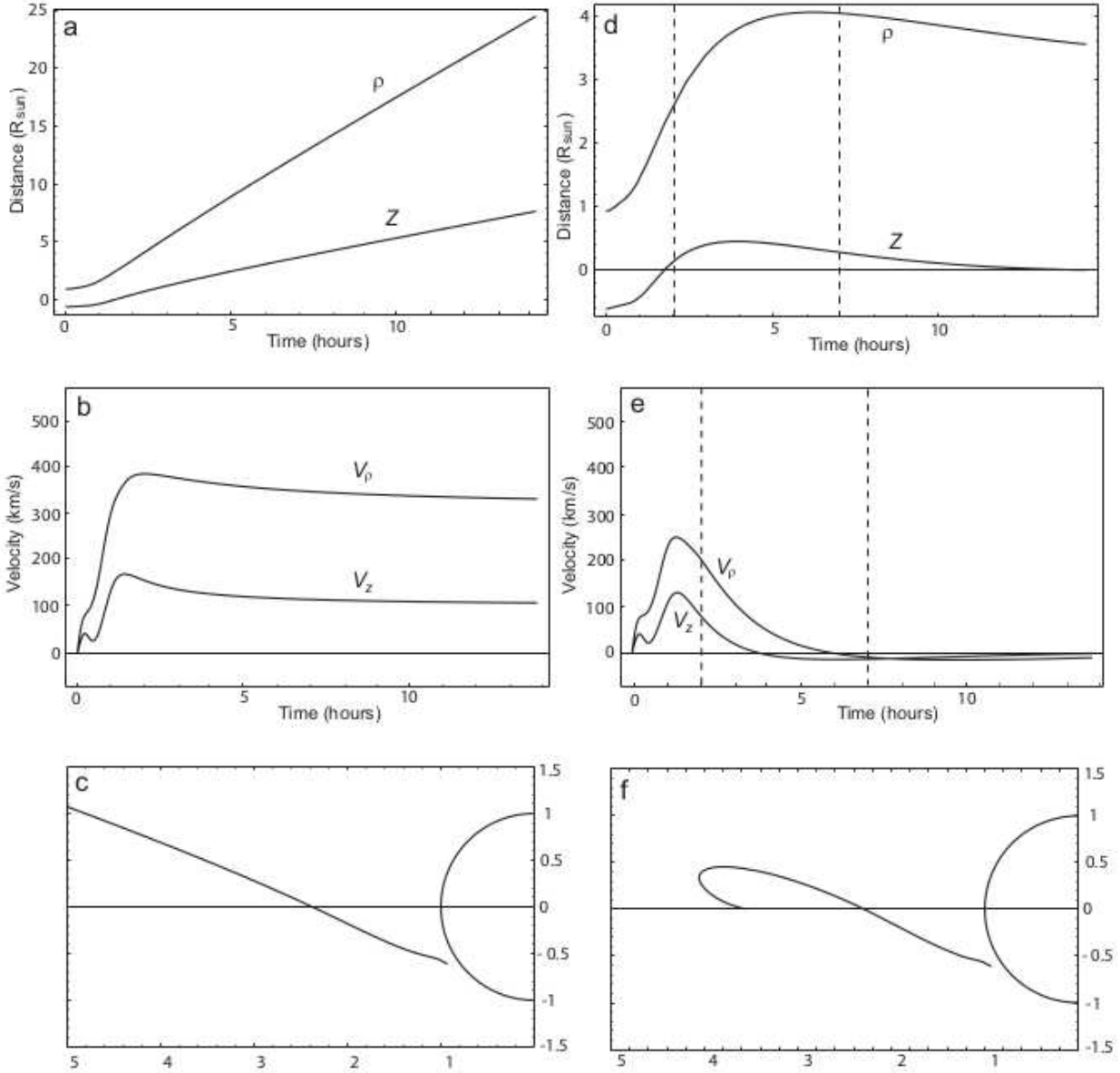


Fig. 11.— The dependence of the flux-rope coordinates, z (top row) and the speed (middle row) on time and the trajectory of the erupting flux-rope motion (bottom row). Left panels correspond to the absence of dissipation, right panels describe the evolution with dissipation.

Table 1: Time-line of the Event.

S.No.	Date (Time)	Observations
1.	17-06-2012 (before 20:30 UT)	Filament is observed on the Sun.
2.	17-06-2012 ($\approx 20:30 - \approx 20:56$ UT)	Slow rise of the filament with the speed around 3 km s^{-1} .
3.	17-06-2012 ($\approx 21:00 - \approx 21:14$ UT)	Fast rise of the filament with the speed around 205 km s^{-1} .
4.	17-06-2012 ($\approx 21:36$ UT)	First appearance of the CME in the LASCO C2 field of view
5.	17-06-2012 ($\approx 22:12$ UT)	First appearance of the CME core in the LASCO C2. Start time of the coronal ray deflection.
6.	17-06-2012 ($\approx 22:36$ UT)	Maximum deflection time of the coronal ray.
7.	17-06-2012 (after $\approx 22:36$ UT)	Returning motion time of the coronal ray.
8.	18-06-2012 (after $\approx 00:48$ UT)	Start time of the downflow of the CME core.